Genetic optimisation of a plane array geometry for beamforming. Application to source localisation in a high speed train

Florent Le Courtois [a,*], Jean-Hugh Thomas [a,b], Franck Poisson [c], Jean-Claude Pascal [a,b]

[a] Laboratoire d'Acoustique de l'Université du Maine (UMR-CNRS 6613), rue O. Messiaen, 72085 Le Mans, France
[b] École Nationale Supérieure d'Ingénieurs du Mans, rue Aristote, 72085 Le Mans, France
[c] Innovation et recherche SNCF, 40 avenue des terroirs de France, 75012 Paris, France

ARTICLE INFO

ABSTRACT

Thanks to its easy implementation and robust performance, beamforming is applied for source localisation in several fields. Its effectiveness depends greatly on the array sensor configuration. This paper introduces a criterion to improve the array beampattern and increase the accuracy of sound source localisation. The beamwidth and the maximum sidelobe level are used to quantify the spatial variation of the beampattern through a new criterion. This criterion is shown to be useful, especially for the localisation of moving sources. A genetic algorithm is proposed for the optimisation of microphone placement. Statistical analysis of the optimised arrays provides original results on the algorithm performance and on the optimal microphone placement. An optimised array is tested to localise the sound sources of a high speed train. The results show an accurate separation.

© 2016 Elsevier Ltd. All rights reserved.

1. Introduction

Noise pollution is a major concern for authorities. The World Health Organization has stated that daily exposure to noise leads to various health issues, such as stress increase, insomnia or cardiovascular problems [1]. Traffic noise is one of the major parts of noise pollution. A deeper knowledge of its sources is required to provide effective acoustic protection and noise reduction solutions. The sound sources are often characterised by their position on the vehicle, their spectra and their relative power.

Array processing has been widely used for imaging acoustic sources in the industrial context. It consists, essentially, in delaying and summing microphone signals to estimate the power coming from one point [2]. The obtained estimate is a convolution of the source distribution and a spatial filter, i.e. the array impulse response or the beampattern. Thanks to its easy implementation and its robustness compared to high resolution methods, the beamforming method is applied commonly for source localisation on trains [3,4], cars [5], airplanes [6] and also wind turbines [7].

In recent years, research in acoustic array processing has proposed many algorithms to improve the imaging results, such as deconvolution algorithms [9,10], CLEAN method [11] and Functional Beamforming [12]. These methods manage to reduce the sidelobes and increase the resolution of the localisation maps.

---

* Corresponding author. Present address: Lab-STICC (UMR CNRS 6285), ENSTA Bretagne (UEB), 2 rue François Verny, 29806 Brest, France. Tel.: +33 2 98 34 89 25; fax: +33 2 98 34 87 50.
E-mail address: florent.le_courtois@ensta-bretagne.fr (F. Le Courtois).

For imaging moving vehicles or rotor blades, the beampattern is then focused on a plane moving with the vehicle to suppress the Doppler effect [8]. The array response is often considered as isotropic, i.e. it does not depend upon the focusing direction. This hypothesis allows deconvolution algorithms to be applied conveniently. This method has been successfully applied on airplanes [6] and wind turbines [7], where the sources are far from the array. In a context of near field propagation (e.g. for imaging trains and cars), the tracking of the sources implies large variation of the beampattern which isotropic property cannot be verified [13,14].

The performance of beamforming depends mainly on the sensor placement (i.e. on the array geometry) [15]. For a given frequency range, wide arrays are known to achieve accurate spatial localisation whereas closely spaced sensors provide low sidelobes [16]. Since these two properties lead to opposite designs, a trade-off has to be made to obtain optimal performance. A relevant placement for linear 1D array was achieved by minimising the redundancy of the inter-microphone distances [17]. The redundancy cannot be expressed for 2D arrays using this method. The study of classical geometry shapes, such as cross [18], star [4], circles [19] or spirals [20,21], are often proposed. The random placement of microphones is considered as a generalisation of the classical shapes [22]. The statistical properties of the mainlobe width and the peak sidelobe level are then investigated.

In this paper, a genetic algorithm (GA) is proposed to solve the problem of finding the geometry that minimises cost functions on the beampattern. The goal is to optimise well known array properties such as the beamwidth, the Maximum Sidelobe Level (MSL) and more complicated criteria that are derived from the classical ones. In particular, the invariance of the beampattern with the focusing direction is studied through an application on moving sources. GA are known to quickly provide good solutions. From a more general point of view, global optimisation algorithms have been suitable to find appropriate geometries [23,24].

The document is organised as follows. In Section 2, the beamforming algorithm is introduced. Array aperture and maximum sidelobe levels are defined. The variation of the beampattern properties with source motion is discussed. In Section 3, the GA used for optimising the sensor position is developed. Cost functions are defined considering the beampattern properties. In Section 4, the results of the optimisation are investigated to validate the convergence of the algorithm and to define the properties of new arrays. In Section 5, Monte-Carlo (MC) simulations are performed to compare the performance of the optimised array with more classical geometries. An application on a high speed train illustrates in Section 6 the localisation improvement of the new geometry.

2. Beamforming

For N_s uncorrelated sources $s_n(t)$ and an array composed of M sensors, the pressure acquired by the mth sensor is expressed as the convolution of the source signals by the impulse response (linked to the Green function) of the medium

$$p_m(t) = \sum_{n=1}^{N_s} s_n(t) * h_{mn}(r_{mn}, t). \tag{1}$$

The impulse response $h_{mn}(r_{mn}, t)$ describes the propagation properties in the medium and r_{mn} is the distance between the nth source and the mth sensor. Considering narrowband sources centred on frequency f, the convolution product of Eq. (1) is expressed in the frequency domain as

$$P_m(f) = \sum_{n=1}^{N} S_n(f) H_{mn}(r_{mn}, f), \tag{2}$$

where $H_{mn}(f)$, $S_n(f)$, $P_m(f)$ are the Fourier transforms of the impulse response of the propagation $h_{mn}(r_{mn}, t)$, the source $s_n(t)$, the pressure $p_m(t)$ respectively. Thus, the received signal on the array can be expressed in the frequency domain as a $[M \times 1]$ vector

$$\mathbf{p}(f) = \mathbf{H}(f)\mathbf{s}(f), \tag{3}$$

where $\mathbf{s}$ is a $N_s \times 1$ source vector and

$$\mathbf{H}(f) = [\mathbf{h}_1(f) \cdots \mathbf{h}_n(f) \cdots \mathbf{h}_{N_s}(f)], \tag{4}$$

is a $M \times N_s$ matrix containing all the impulse response vectors. $H_{mn}(r_{mn}, f)$ is the mth element of $\mathbf{h}_n(f)$. Considering some hypothesis on the medium and the sources, a propagation model is defined. For point sources with spherical propagation in a homogenous free field and isotropic medium, the transfer function describing the sound propagation from the nth source to the mth microphone is expressed as [25]

$$H_{mn}(r_{mn}, f) = \frac{1}{4\pi r_{mn}} \exp\left(-2j\pi f \frac{r_{mn}}{c}\right). \tag{5}$$

c is the sound speed and r_{mn} the distance between the nth source and the mth microphone. $H_{mn}(r_{mn}, f)$ corresponds then to a phase shift (or a delay of r_{mn}/c in the time domain) and a geometrical attenuation of the sources. Beamforming considers the propagation effects by applying a steering vector $\mathbf{w}_n^H$ on the measurements and estimating the nth source amplitude, ^{H} denotes the Hermitian operator. The dimension of $\mathbf{w}_n^H$ is $1 \times M$. The mth element of $\mathbf{w}_n^H$ is defined as

$$W_{mn}(r_{mn}, f) = \frac{\exp(2j\pi f r_{mn}/c)}{4\pi r_{mn}} = H_{mn}^*(r_{mn}, f), \tag{6}$$
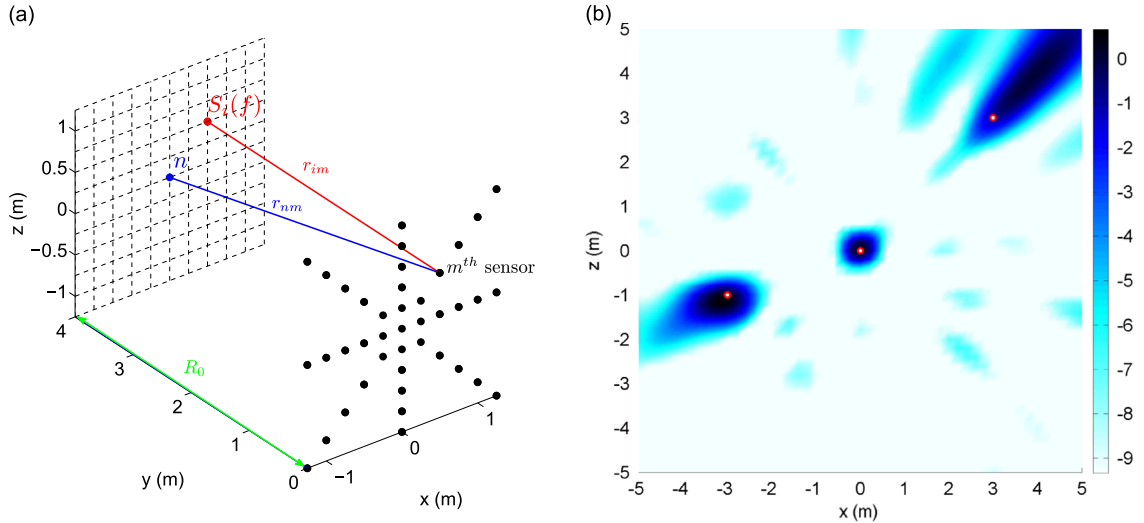
(a)

(b)

Fig. 1. (a) 41-sensor star array and (b) beamforming estimate for three harmonic sources of same level at 600 Hz located at the red points. The map highlights the amplitude of the source distribution normalised by the theoretical amplitude of the sources in the range [− 9 0] dB. (For interpretation of the references to colour in this figure caption, the reader is referred to the web version of this paper.)
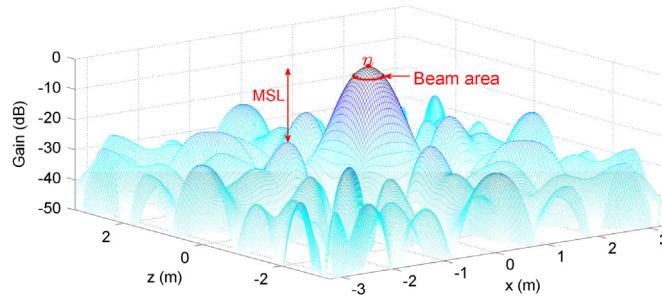

Fig. 2. Beampattern of the star array at 800 Hz. The mainlobe indicates the focus direction n in [0 0]. Beampattern is characterised by the width of its main lobe and the level of the secondary lobes (MSL).

*denotes the conjugate operator. The beamforming process gives an estimate of the nth source amplitude

$$\hat{s}_n(f) = Q\mathbf{w}_n^H(f)\mathbf{p}(f) = Q\mathbf{w}_n^H(f)\mathbf{H}(f)\mathbf{s}(f), \tag{7}$$

where $Q = \sum_{m=1}^{M}(4\pi r_{mn})^2$ is a normalisation factor.

As an example, a simulation is run using a star array of 41 sensor elements shown in Fig. 1(a). The estimate of the source levels for 3 harmonic sources of same sound power at 600 Hz is plotted in Fig. 1(b). The actual source positions are indicated by the red points and the dynamic range is 10 dB, normalised by the theoretical amplitude of the sources. The source level is approximately 1 dB overestimated. The size of the spot around a maximum can be seen as a localisation resolution for the given dynamic range. Except for the source in the upper right corner at [3 3], the maxima correspond to the source positions. The shapes of the peaks are linked to the interaction between the source directivity and the beampattern of the array, which becomes distorted when the sources are not in front of the centre of the array: peaks from sources which are not in front of the array have oval shapes whereas the centred source is delimited by a circle shape. Also, interference appears on the map, which disturbs the interpretation of the results and could lead to misinterpretation of the physics. Those estimation artefacts are created by the array sidelobes and the beamforming algorithm.

2.1. Beampattern

In Eq. (7), the product $\mathbf{w}_n^H(f)\mathbf{H}(f)$ indicates the source contribution to the beamform map of the nth source. Let us define

$$D_{ni}(f) = |\mathbf{w}_n^H(f)\mathbf{h}_i(f)|^2, \tag{8}$$

as the array response focused on n for a source located in i. This function describes the beampattern, with the main lobe pointing in the focusing direction, as shown in Fig. 2. Estimation of the nth source level depends on the beampattern ability to reject the contribution of the other sources. Beamforming is equivalent to a spatial filter.

The beampattern indicates the quality of the beamforming estimation: the narrower the main lobe, the more accurate the spatial localisation of the source and the smaller the secondary lobes, the less energy the other sources contribute.
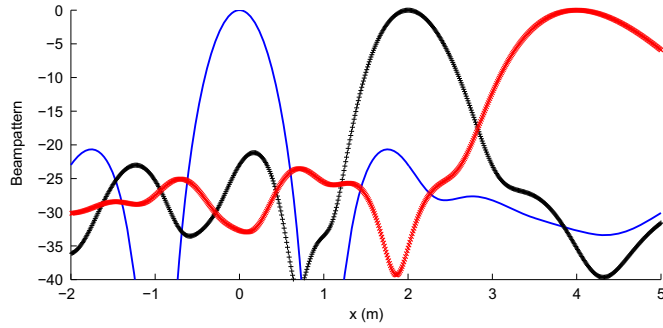
Fig. 3. Beampattern cross-section for the focussing in abscissa 0 m $(-)$, 2 m $(+)$, and 4 m $(\times)$.

Criteria associated with beampattern properties can be proposed to characterise the performance of the array. The area on the plane at -3 dB under the maximum of the main lobe is defined as the array beam area (see Fig. 2) [15]:

$$c_{\mathrm{ap}} = \sum_{l=1}^{N_x} \sum_{j=1}^{N_z} \begin{cases} 1 & \text{if } D_{ni}(f,l,j) \geq -3 \text{ dB} \\ 0 & \text{if } D_{ni}(f,l,j) < -3 \text{ dB,} \end{cases} \tag{9}$$

where N_x and N_z are the numbers of elements in the focussing plane in x and z directions, $N_x \times N_z = N_s$. c_{ap} is an area expressed in pixels and can be defined in square meters. A low c_{ap} leads to a high spatial resolution. At a given frequency, this property is essentially dependent on the array length, the more widely spaced the microphones, the smaller the beam width [25]. The Maximum Sidelobe Level (MSL) was introduced as the level of the main secondary lobe [15]. MSL is generally expressed in dB. The linear measurement, Eq. (10), is introduced

$$c_{\mathrm{MSL}} = \frac{A_0}{A_2} = 10^{\frac{\mathrm{MSL}}{20}}, \tag{10}$$

where A_0 and A_2 are respectively the main lobe amplitude and the greatest secondary lobe amplitude. It indicates the ability of the array to reject the contribution of the sources that are not in the direction of the focusing point. The greater the MSL, the more the array rejects the contribution from the other directions. Unlike the array aperture, a high MSL is achieved by reducing the sensor inter-space [15].

As Eq. (8) depends also on the focusing point position n, Fig. 3 shows the beampattern cross-section for focusing in $x = 0$ m $(-)$, 2 m $(+)$, and 4 m $(\times)$. Depending on the focusing, the beampattern is different, which leads to different values of c_{ap} and c_{MSL}. The variation can be quantified by the root mean squared value of the difference between the mean value $\bar{c}$ computed from different focusing directions in the reconstruction plane and the value c_n associated with the focusing point position n:

$$\sigma_c = \sqrt{\frac{1}{N_s} \sum_{n=1}^{N_s} (\bar{c} - c_n)^2}. \tag{11}$$

Then, a low σ_c implies that the beampattern property characterised by c does not vary much with the direction. This property is important for source tracking to suppress the Doppler effect [8]; in this case the focus point follows the trajectory of the vehicle, so the variation of the beampattern directly impacts the characterisation of the source. The variation also impacts the source representation, as in Fig. 1(b) where sources appear distorted. This effect is mainly noticeable in the context of sources in motion.

2.2. Beamforming for moving sources

For imaging moving sources, the beamforming process is modified [8]: the focusing plane moves with the vehicle. The distance between the source and the sensor in the impulse response, Eq. (1), is now time dependent

$$p_m(t) = \sum_{n=1}^{N_s} s_n(t) * h_{mn}(r_{mn}(t), t), \tag{12}$$

where, in the case of an omnidirectional source,

$$h_{mn}(r_{mn}(t), t) = \frac{\delta\left(t - \frac{r_{mn}(t)}{c}\right)}{4\pi r_{mn}(t)}, \tag{13}$$

and δ is the Dirac distribution. The motion creates a non-uniform sampling of the emitted data. It generates a modulation of the received frequency: the Doppler effect.

The so-called dedopplerisation operation consists in focusing the array on the source trajectory for a short time. Then, the time domain beamforming becomes

$$\hat{s}_n(t) = \sum_{m=1}^{M} p_m(t) * w_{nm}(r_{mn}(t), t).$$ (14)

with the steering vector

$$w_{mn}(r_{mn}(t), t) = \frac{1}{\Xi(t)} \frac{\delta\left(t + \frac{r_{mn}(t)}{c}\right)}{4\pi r_{mn}(t)},$$ (15)

where $\Xi(t)$ is a normalisation coefficient. It is equivalent to an interpolation of the received data in the emission time; the Doppler effect is then corrected [8]. Some a priori information concerning the speed and direction of the source motion is required. Examples of dedopplerisation can be found for circular [7] or rectilinear [3] known motion.

Consider harmonic and omnidirectional moving sources. Since the beampattern depends on the focusing point n, as shown in Eq. (8) and in Fig. 3, the spectrum of the time signal reconstructed by beamforming no longer exhibits a single frequency peak. For example, a simulation is run with two sources of same level at 800 Hz, separated by 1 m and moving at 360 km/h. The sources are at the same height: the middle of the array. The minimum distance between the sources and the array is 4 m. No additive noise is considered in this case. The source time signals estimated from Eq. (14) are plotted in Fig. 4(a) for a tracking of the passing by on 6 m or 60°. The resulting frequency resolution is $\Delta_f = 14$ Hz. Interference between the two sources and the beampattern leads to amplitude modulation. The non-stationarity of the beamforming for moving sources is exhibited. In addition, the spectra computed in Fig. 4(b) reveal wider peaks around 850 Hz and 750 Hz that correspond to the Doppler modulated frequency of the other source. Note that, due to the short tracking duration, the frequency resolution is quite poor. For practical applications, the bias induced by the method is reduced by computing the Welch periodogram of signal $\hat{s}_n(t)$, but the frequency resolution becomes greatly downgraded.

These simple cases illustrate that interference between sources and the array response impacts the results, especially concerning moving sources. The criteria, introduced in Section 2.1, could be used to evaluate the array performance. The array design problem is to find the microphone positions that optimise the array performance given by one or several of the previously defined criteria. The use of a GA is proposed in the next section for the optimisation.

3. Genetic optimisation

The optimisation process consists in finding the microphone positions that will provide the best array performance according to c_{ap}, c_{MSL} and other properties previously introduced. Since the sensor positions do not appear in the criterion expressions and since a lot of possibilities have to be tested, linear optimisation cannot be applied. A global optimisation algorithm is required.

Inspired by Darwin's natural selection principle, GA were proposed by Holland [26]. They proved their efficiency in several engineering domains and also in array optimisation [23]. They are known for providing rapidly (after few iterations) optimised solutions but due to random generations, solutions could differ from one run to another [27]. A population of solutions is considered for which

- The individuals differ,
- Their specificities are coded in their genome,
- Only the best individuals survive and transmit their abilities to their children.

In the context of geometry optimisation, an individual is an array geometry i.e. a set of a given number (29 for the
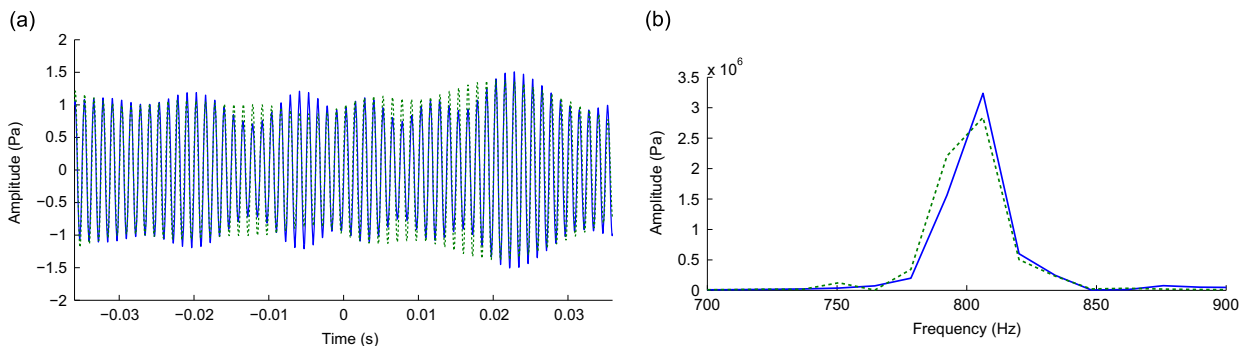

Fig. 4. (a) Estimated time signals and (b) their spectra from two moving sources (same level, 800 Hz, separated by 1 m) with a tracking on 60°. The signals in (a), computed from Eq. (14), highlight source interference.
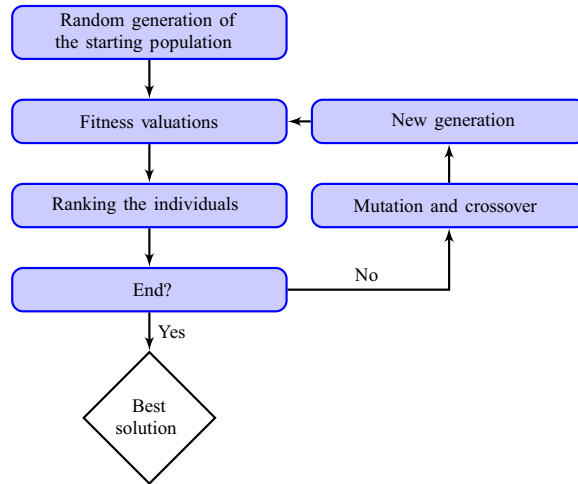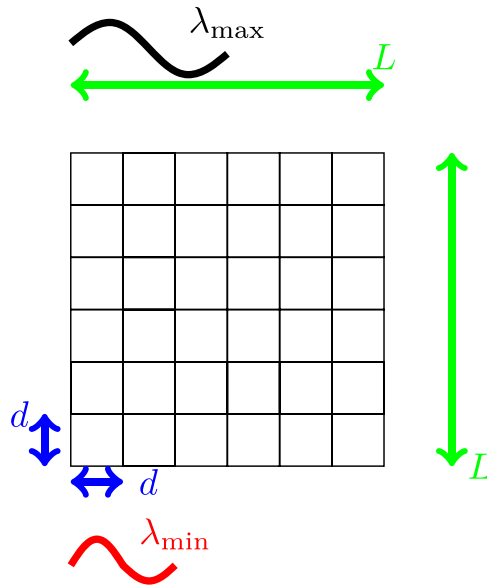
Fig. 5. Genetic algorithm.

Fig. 6. Array mesh definition for the wavelength bandwidth [λ_{min} λ_{max}].

simulations, 41 for the experiment) of microphones with their coordinates, the genes are the microphone positions and the abilities are the criteria, or fitness functions, c_{ap} and c_{MSL}.

The optimisation process is described by the flowchart plotted in Fig. 5. The first step is to generate random individuals. Each of them is evaluated using a cost function. The individuals are sorted from the best to worst. The mutation and the crossover are two operations, described in the next section, for the population replacement. Children are generated, then evaluated, and sorted as well. The algorithm is iterated and due to the selection, individuals become more suitable at each generation.

3.1. Application to the array optimisation problem

Several algorithms were developed for genetic optimisation [26,27] with different characteristics (binary genomes, sub-populations, populations with different sizes, with or without crossover) adapted to different problems. In this section, an algorithm dedicated to the array geometry optimisation is described.

To generate random geometries (i.e. individuals), a discrete mesh of possible microphone positions is proposed. This configuration is easy to realise and allows a lot of geometries. For a frequency bandwidth [f_{min} f_{max}], the grid step d is defined by the Nyquist–Shannon sampling theorem $d \leq c/(2f_{max}) = \lambda_{min}/2$. Spatial aliases would occur if d were larger than $\lambda_{min}/2$. This gives an upper limit for d. The array aperture, L, is chosen so that $L \approx 2c/f_{min} = 2\lambda_{max}$ and L/d is an integer. Microphones are placed on the intersections of the mesh shown in Fig. 6. Such an array provides $(L/d+1)^2$ possible
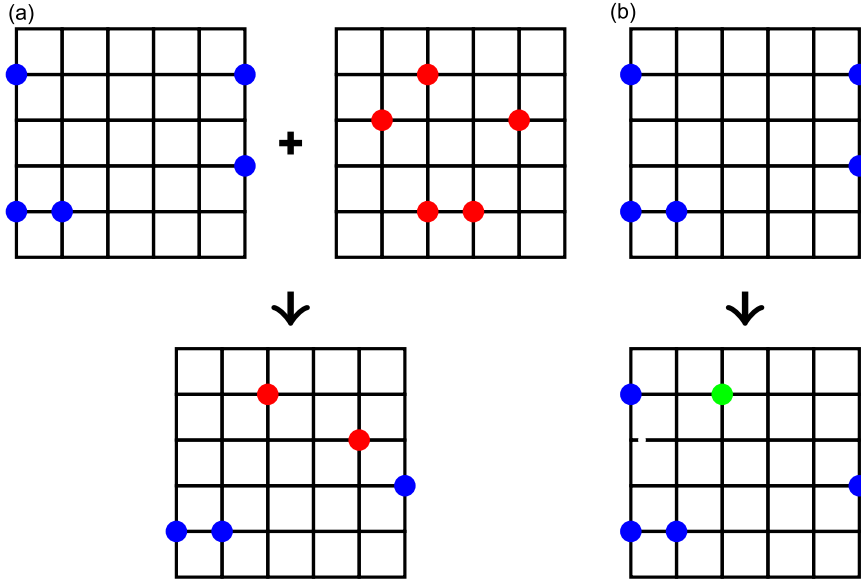
Fig. 7. (a) Crossover operation, microphone positions are moved from an array to another, and (b) mutation operation, a microphone position is randomly replaced by a new random position.

microphone placements and

$$C^M_{(\frac{L}{d}+1)^2} = \frac{\left(\frac{L}{d}+1\right)^2!}{\left(\left(\frac{L}{d}+1\right)^2 - M\right)!M!} \tag{16}$$

geometries. For example, placing 29 microphones for the bandwidth [200 700] Hz provides 3.82×10^{34} combinations. Investigation of all combinations is not feasible.

New arrays are generated from the starting generation using two operators. The crossover is an operation for transmitting parents' genes to the offspring, as shown in Fig. 7(a). In this context, a gene is a microphone location. For the randomly selected couple of solutions i and j, with the respective normalised fitness evaluations e_i and e_j, the probability that the mth gene of the child is received from parent i is:

$$P(c_{i,j,m}) = \text{Prob}(\alpha(m) < e_i \times (1 - e_j)), \tag{17}$$

where $\alpha(m)$ is a random number uniformly drawn in [0 1]. Otherwise, the child received the gene from parent j. This operation favours the gene transmission of the most adapted parent. The crossover operation helps the population to converge.

The mutation operation is the substitution of one random microphone position by another one randomly chosen, as shown in Fig. 7(b). The eventuality of the mutation of the mth gene of the ith individual is defined by the probability

$$P(\text{mut}_{i,m}) = \text{Prob}(\beta(m) < b), \tag{18}$$

where $\beta(m)$ is a random number uniformly drawn in [0 1] and b is a mutation parameter. Mutation is a random operation which helps the algorithm to explore the solution space.

The population size does not change during the algorithm computation; at each new generation, the child number equals the parent number.

3.2. Aggregation of criteria

As seen in Eqs. (9) and (10), c_{ap} needs to be minimised and c_{MSL} to be maximised to provide a global performance. It is a so-called multi-objective optimisation. The global solution of a multi-objective optimisation can be achieved by several methods [28]. The optimum can be defined as the solution that will downgrade the less the performance [27]. A normalised summation of the criteria may be used but it requires a priori information on the performance scale. A multiplicative aggregation of the criteria may be used to avoid the normalisation [27]. A new criterion to optimise both criteria c_{ap} and c_{MSL} is defined as

$$c_{ag} = \frac{c_{ap}}{c_{MSL}}. \tag{19}$$

The minimisation of c_{ag} may lead to a simultaneous optimisation of c_{ap} and c_{MSL}. Note that, for critical cases, favouring one criterion can provide degenerate solutions. However, in the context of a low spatial variance of the beampattern [see Eq. (11)],

Table 1
Parameters used for the optimisation of the array geometry.

Parameters	Values
f_{min}	200 Hz
f_{max}	700 Hz
L	3.16 m
d	0.24 m
M	29
b	0.01
Number of individuals	100
Number of generations	100

the multiplicative aggregation provides a simple cost function c_{iso}

$$c_{iso} = \epsilon_{ap}\epsilon_{MSL}, \tag{20}$$

where

$$\epsilon_{ap} = \frac{\sigma_{ap}}{\bar{c}_{ap}} \quad \text{and} \quad \epsilon_{MSL} = \frac{\sigma_{MSL}}{\bar{c}_{MSL}} \tag{21}$$

are the relative variances of c_{ap} and c_{MSL}. The optimisation of c_{iso} leads to the minimisation of the performance variation of the focusing plane.

Finally, this paper considers four cost functions to optimise: the minimisation of c_{ap}, c_{ag} and c_{iso} respectively defined in Eqs. (9), (19) and (20) and the maximisation of c_{MSL}, in Eq. (10).

4. Optimisation results

The algorithm convergence depends on the cost functions, the mutation and crossover parameters, the population size, and the number of genes and generations. The only way to verify the ability of the algorithm to provide optimised and repeatable solutions with the selected parameters is to investigate the statistics of many optimised solutions [27]. In this section, the repeatability of the sensor positions and the performance are investigated for 100 arrays optimised in c_{ap}, c_{MSL}, c_{ag} and c_{iso}. The objective is to validate the optimisation process and also to identify trends. The parameters used for this example are listed in Table 1.

First the focus is made on the performance of the arrays in terms of sidelobe level and beamwidth for a focusing facing the centre of the array. Then, the sensor placement obtained by the four criterion optimisations is investigated. The c_{iso} criterion, in particular, takes into account each focusing point of the reconstructed mesh. Finally, the sensitivity of the optimised array to the frequency is studied.

4.1. Convergence of the performance

As mentioned in the Introduction, the beamwidth and the MSL are generally considered to evaluate array performance. In this part, c_{ap} and c_{MSL}, defined in Eqs. (9) and (10), are used to compute the theoretical performance of the optimised array. Considering the 100 arrays optimised per criterion, the distribution of the performance indicates the robustness of the algorithm, i.e. its capacity to recover an identical solution on each run.

The evaluation distribution on the $(1/c_{MSL}, c_{ap})$ plane and the associated marginal distribution are plotted in Fig. 8. Note that the axes are normalised and the abscissa is the reciprocal of c_{MSL}; thus 1 represents the worst performance and 0 the best. The c_{ap} optimised arrays are indicated by $\times$, the c_{MSL} by $+$ and the c_{ag} by $\circ$. The histograms of the performance are plotted along the abscissa for c_{ap} and the ordinates for $1/c_{MSL}$.

The distribution of the criteria when c_{ap} is optimised indicates homogenous results concentrated near the best result on the c_{ap} axis but they are spread on the c_{MSL} axis. The criteria obtained when c_{MSL} is optimised are widely distributed among the c_{ap} axis and concentrated next to the best value on the $1/c_{MSL}$ axis. However, the c_{MSL} criterion varies in a larger interval over its optimised axis than the c_{ap} one. The c_{ap} criterion seems to be more difficult to optimise. It is obvious that the single criterion optimisation of c_{MSL} or c_{ap} downgrades the other criterion. The optimised array using c_{ag} tends to find a trade-off between both criteria.

4.2. Convergence of the sensor placement

As the optimised arrays produce some repeatability in their performance, the purpose is to discern preferential positioning for sensors, associated with the given cost functions that are to be optimised by the GA. The microphone placement distribution is plotted in Fig. 9(a), (b), (c) and (d), respectively for 100 arrays optimised in c_{ap}, c_{MSL}, c_{ag} and c_{iso}. The darker the position, the more often the position is chosen by the algorithm as an optimal placement. The array with the best performance for its optimisation criterion is indicated with $\bullet$.
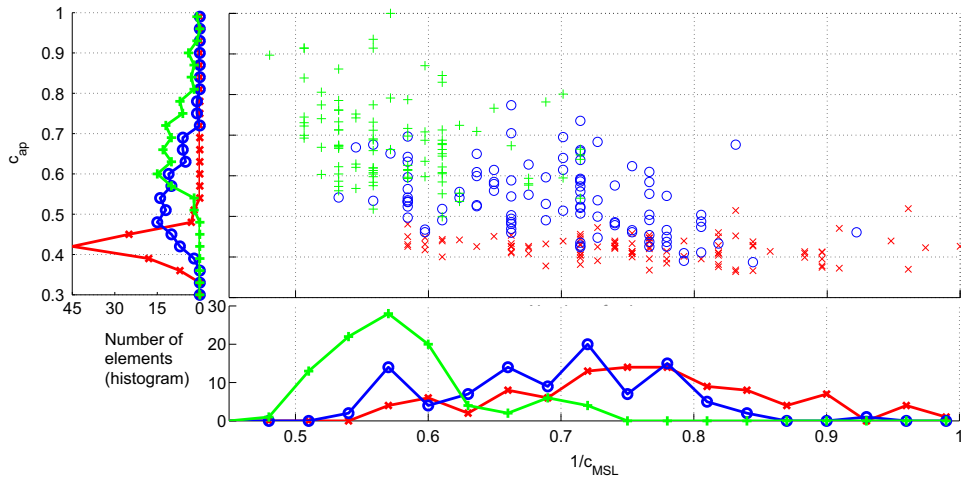
Fig. 8. Evaluation of the optimised array performance on the $(1/c_{MSL}, c_{ap})$ plane. The $\times$ highlight the performance of the c_{ap} optimised arrays, $\circ$ show the performance of the c_{ag} optimised array and the $+$, the performance of the c_{MSL} optimised array. The respective histograms of the evaluation are plotted along the axis. Data are normalised by the worst performance.
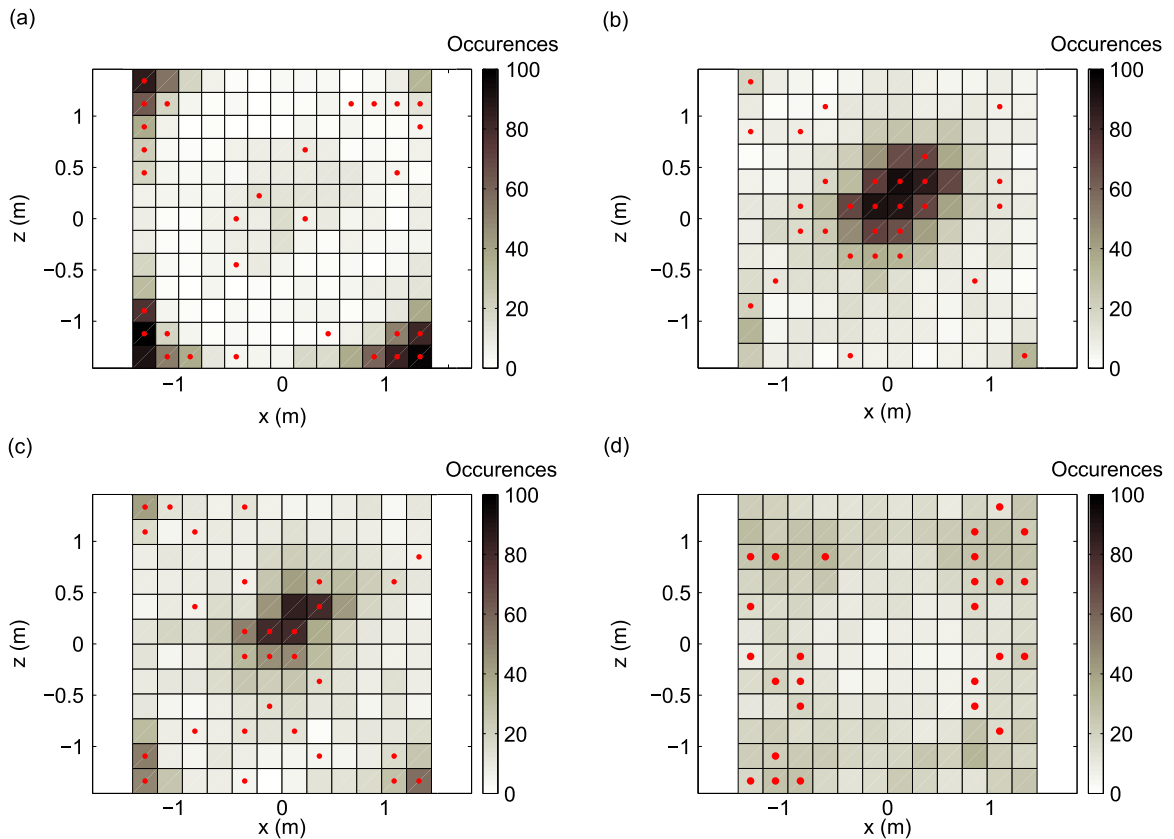

Fig. 9. Occurrence of the microphone positions on 100 optimised array for criteria (a) c_{ap}, (b) c_{MSL}, (c) c_{ag} and (d) c_{iso} ($M=29$, $L=3.16$ m, $d=0.24$ m). The microphone positions for the best array among the 100 optimised are indicated by the $\bullet$.

For c_{ap} optimisation, centred microphones are avoided, they are placed at the corner to minimise the criterion. On the contrary, c_{MSL} optimisation gathers microphones at the array centre. The c_{ag} optimisation produces a compromise of the c_{ap} and c_{MSL} geometries: microphones are at the centre and in the corners of the grid.

The observed geometry tendencies are consistent with observations [16,20]: increasing the space between microphones enhances the discrimination ability of the array and concentrating the microphones leads to low side lobes. The geometries
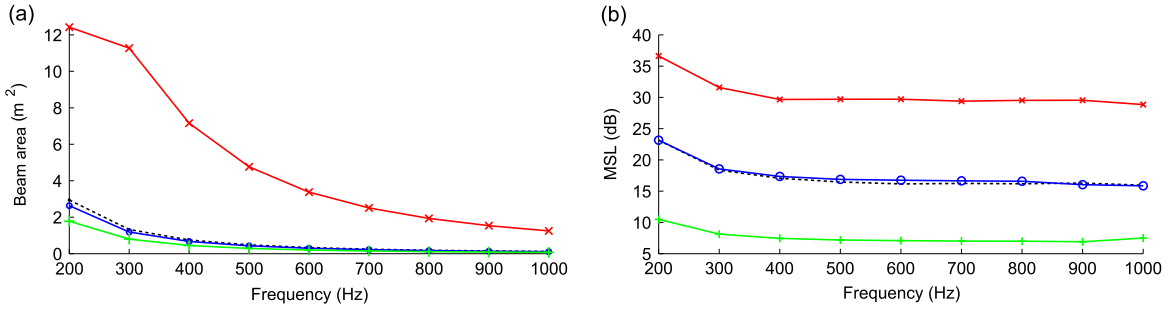
Fig. 10. Evolution over the frequency bandwidth of (a) the beamwidth and (b) the MSL for c_{ap}, c_{MSL}, c_{ag} and c_{iso} arrays in $+$, $\times$, $\circ$, and $--$ respectively.

obtained by optimisation can then be compared to more classical shapes: c_{ag} optimisation leads to a microphone positioning close to a star, a cross or a spiral shape.

For c_{iso} optimisation (see Fig. 9(d)), the position occurrence is lower than for the other arrays: the most occupied positions are common for 30 percent of the optimised arrays, which is low in comparison with the other criteria. It is possible that c_{iso} is a more sensible criterion to optimise and the solution space has a lot of local solutions. From a general point of view, the algorithm tends to avoid central position. The microphone distribution seems to be circular but the interpretation is difficult. The best array appears to be composed of two sub-arrays with similar geometries.

4.3. Criterion evolution with the frequency

As the arrays are designed for a frequency bandwidth, the evolution of the criteria with frequency is of great interest to validate the geometry. For the best array optimised in the previous subsection, the values of c_{ap} and c_{MSL} for the arrays are computed at several frequencies. The frequency bandwidth studied is [200 1000] Hz which is a little wider than the frequency bandwidth used before. The criteria are calculated for a focusing in front of the centre of the defined mesh. This configuration is used for the optimisation for c_{ap}, c_{MSL} and c_{ag} arrays. The optimisation for c_{iso} takes into account the focusing on each point of the mesh. Both c_{ap} and c_{MSL} criteria are plotted as a function of the frequency in Fig. 10(a) and (b) for c_{ap}, c_{MSL}, c_{ag} and c_{iso} arrays, respectively in $\times$, $+$, $\circ$ and dashed line.

The c_{MSL} optimised array provides the greatest MSL level and the worst beamwidth on the overall bandwidth. In the same way, the c_{ap} optimised array has a small beam area and significant sidelobes at all frequencies. The two other arrays present compromised performance as expected.

According to Christensen and Hald [15], a MSL above 10 dB is a good performance. The optimisation of c_{MSL} alone or in a multi-objective framework provides arrays with low sidelobe levels. The resolution of the arrays, excepted for the c_{MSL} optimised one, is in the order of the source distances (for instance 3 m between the wheels of TGV) found on the vehicles (cars and trains).

4.4. Criterion evolution with the focusing position

As mentioned, the arrays optimised in c_{ap}, c_{MSL} and c_{ag} considered only one focusing point in front of the array. The c_{iso} array is optimised for several focusing points. In this section, the beampattern is focused on a 2D mesh between -2 m and 2 m with an inter-space of 5 cm in both dimensions at 600 Hz. The mean and the standard deviation of c_{ap}, c_{MSL} and the evaluation of c_{iso} for each array over all focusing points are indicated in Table 2.

The arrays optimised in c_{ap} and c_{MSL} provide the best averaged performance in their respective criteria. However, when several focusing points are taken into account, the c_{iso} array performs better that c_{ag} array in the spatial averaged $\bar{c}_{ap}$ and $\bar{c}_{MSL}$ criteria. In addition, the c_{iso} array has the lowest standard deviation $\sigma_{c_{ap}}$ and the second lowest $\sigma_{c_{MSL}}$.

The lowest $\sigma_{c_{MSL}}$ is obtained by the c_{ap} array optimised. In a more general perspective, the variation on the performance of the c_{ap} array is low, in contrast to the c_{MSL} array. This remark is consistent with the sensor distribution in Fig. 9: concentrated sensors lead to poor performance when focusing in several directions.

4.5. Simulation

The optimised arrays indicated by the red points in Fig. 9(a)–(d) are tested by simulation to assess their usefulness in terms of localisation. Two harmonic sources at 600 Hz with same level are generated. The beamforming results are plotted for optimised arrays according to c_{ap}, c_{MSL}, c_{ag} and c_{iso} in Fig. 11(a), (b), (c) and (d) respectively.

Referring to Fig. 11, c_{iso} is clearly the best in terms of source location accuracy and freedom from artefacts for general source locations. c_{iso} is investigated in the next section.

Table 2
Mean and standard deviation on the array performance of the optimised arrays at 600 Hz over the focusing points of the mesh.

Valuation	c_{ap}	c_{MSL}	c_{ag}	c_{iso}
$\bar{c}_{ap}$ (m^2)	0.27	2.57	0.33	0.28
σ_{ap} (m^2)	0.18	0.61	0.21	0.08
$\bar{c}_{MSL}$ (∅)	1.90	49.23	4.88	4.96
σ_{MSL} (∅)	0.39	15.29	1.75	1.55
c_{iso} (∅)	0.14	0.74	0.23	0.08
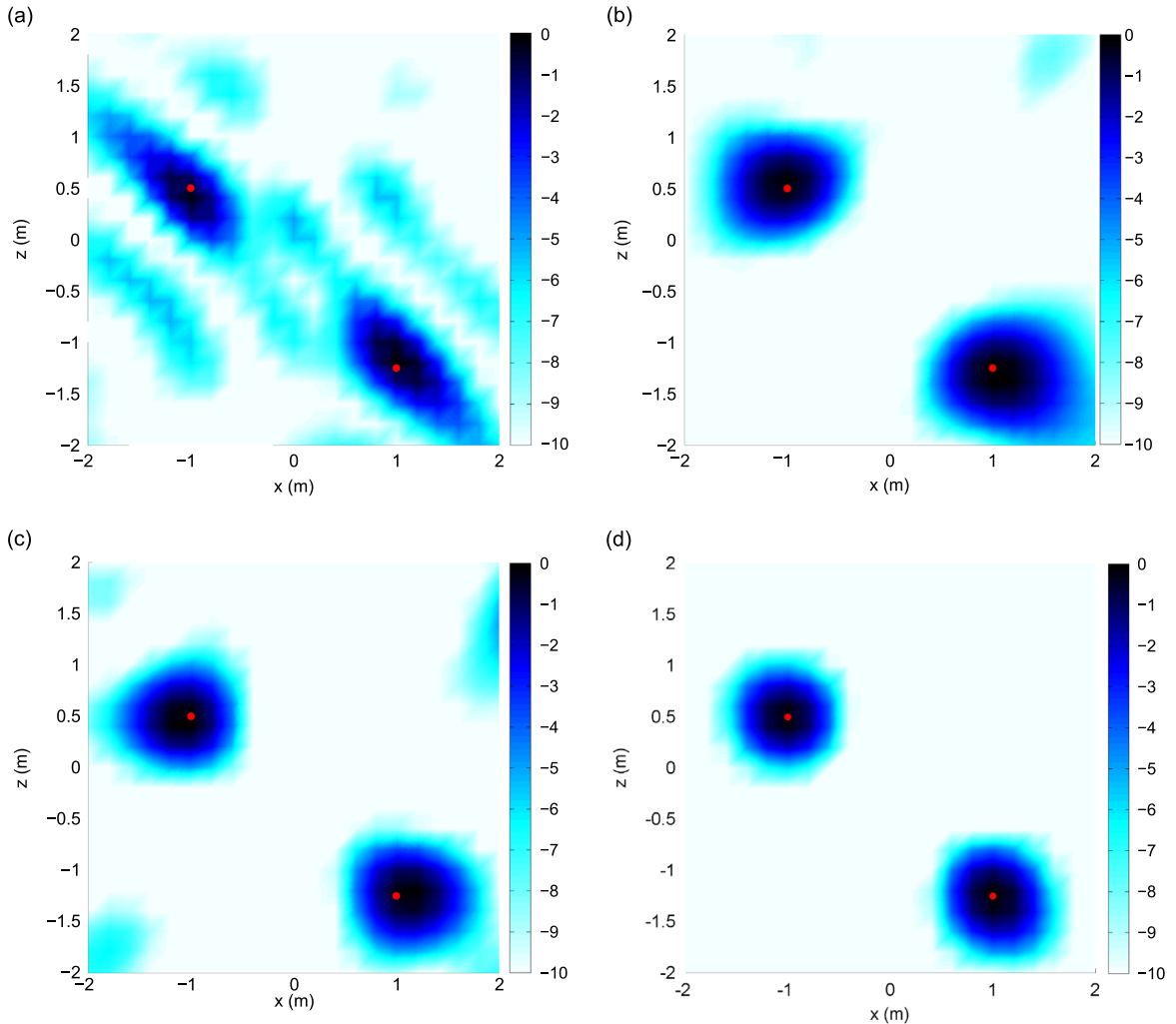
Fig. 11. Beamforming results for two harmonic sources of 600 Hz, located by the ●, using arrays optimised according to (a) c_{ap}, (b) c_{MSL}, (c) c_{ag} and (d) c_{iso}.

5. Source separation performance of the c_{iso} optimised array

This section proposes to validate the impact of the c_{iso} beampattern optimisation on the source location. In the first part, the power of resolution is investigated in Monte-Carlo (MC) simulations. In the second part, the particular case of moving sources is studied by analysing the ability of the array to correct the Doppler effect.

For this study, the 41-sensor array is optimised for the c_{iso} criterion in the [200, 1200] Hz bandwidth providing the geometry in Fig. 12(a). The same tests are performed using the star array in Fig. 1(a), and the one-arm-spiral array in Fig. 12 (b), to compare the performance. Those arrays are composed of 41 sensors, with a 3 m aperture.

5.1. Power of resolution

The resolution defines the minimal distance to discriminate two sources. To estimate the resolution of the arrays, MC simulation is proposed: a source is randomly drawn on a plane; a second source is randomly drawn at a determined distance d from the first
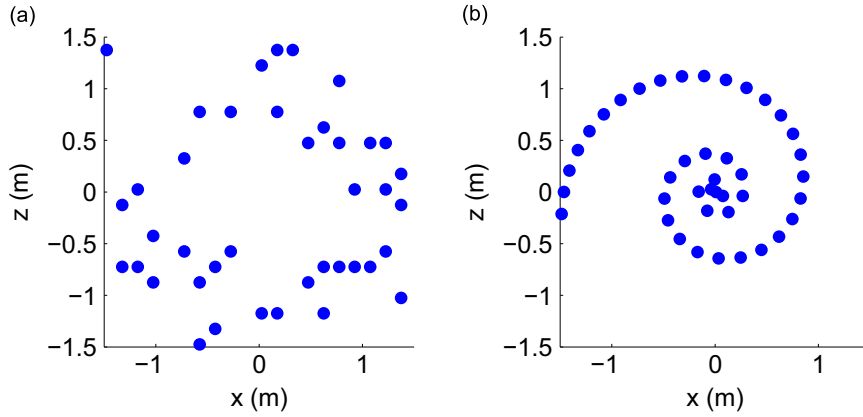
Fig. 12. (a) c_{iso} optimised array in the [200, 1200] Hz bandwidth and (b) one branch spiral array.
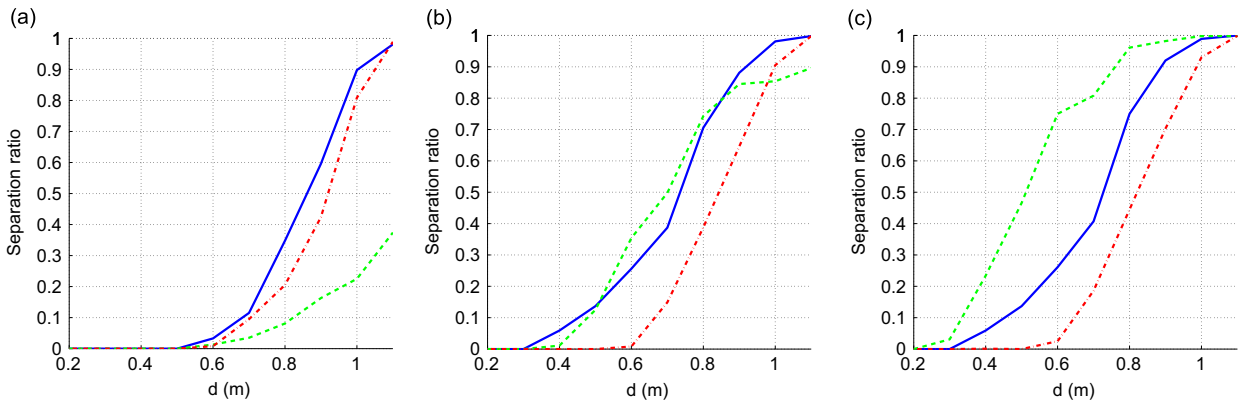

Fig. 13. Separation ratio of two sources of same level with a 10 dB SNR for 1000 MC simulations for the c_{iso} optimised array (—), the spiral array (— —) and the star array (—•—) at frequencies (a) 600 Hz, (b) 1000 Hz and (c) 1200 Hz.

one. The beamforming is performed with 0.2 m interspace in the mesh. If the maxima of the beamforming are located at the true position of the sources, with respect to the mesh accuracy, the separation is notified. Otherwise the array does not distinguish between the two sources. A binary value is obtained for each configuration: 1 if the separation is done, 0 otherwise.

The separation is estimated at 600 Hz, 1000 Hz and 1200 Hz; the corresponding wavelengths are $\lambda_{600} = 0.56$ m, $\lambda_{1000} = 0.34$ m and $\lambda_{1200} = 0.28$ m. White noise is added to the simulated acoustic signals with a signal-to-noise ratio (SNR) of 10 dB. The distance between the two sources runs from 0.2 m to 1.1 m in steps of 0.1 m. For each value, 1000 simulations are performed.

Fig. 13(a) indicates the separation ratios (1 means 100 percent of recognition of the right source positions) at 600 Hz for the c_{iso} optimised array in –, the star array in –•– and the spiral array in – –. For all the arrays, 0.5 m (0.87 λ_{600}) is the smallest distance retrieved between two sources. The smallest distance to separate safely two sources is 1.1 m (1.92 λ_{600}) for the c_{iso} optimised array and the star array; at 600 Hz, the separation rate is too low for the spiral array. At this frequency, the c_{iso} optimised array is the most able to separate two sources.

The same test is run at 1000 Hz and the results are displayed in Fig. 13(b). The smallest separation distance achieved is 0.3 m (0.87 λ_{1000}) for the c_{iso} optimised and spiral arrays and 0.6 m (1.75 λ_{1000}) for the star array. 100 percent of separation is performed when the sources are separated from 1.1 m (3.21 λ_{1000}) for the c_{iso} optimised and the star array. However, the c_{iso} array achieves a 90 percent separation rate for sources distant from 0.88 m (2.56 λ_{1000}) which is 0.1 m (0.29 λ_{1000}) smaller than the distance required by the star array for the 90 percent ratio. The optimised array provides a better separation ratio overall.

Finally, the ratio is computed at 1200 Hz and plotted in Fig. 13(c). The spiral array is the most efficient one, achieving the smallest resolution of 0.2 m (0.70 λ_{1200}) and 100 percent separation at 1.1 m (3.85 λ_{1200}). The ratio of the other arrays is slightly improved but remains close to the performance at 1000 Hz.

In the [200 1200] Hz bandwidth, the most able to separate the sources is the array optimised with respect to the c_{iso} criterion.

5.2. Frequency estimate of moving source

Since the Doppler frequency in dedopplerised spectrum is related to the separation ability and variation of the array beampattern (see Section 2), a similar MC approach is proposed for estimating the emitting frequency of a moving source.
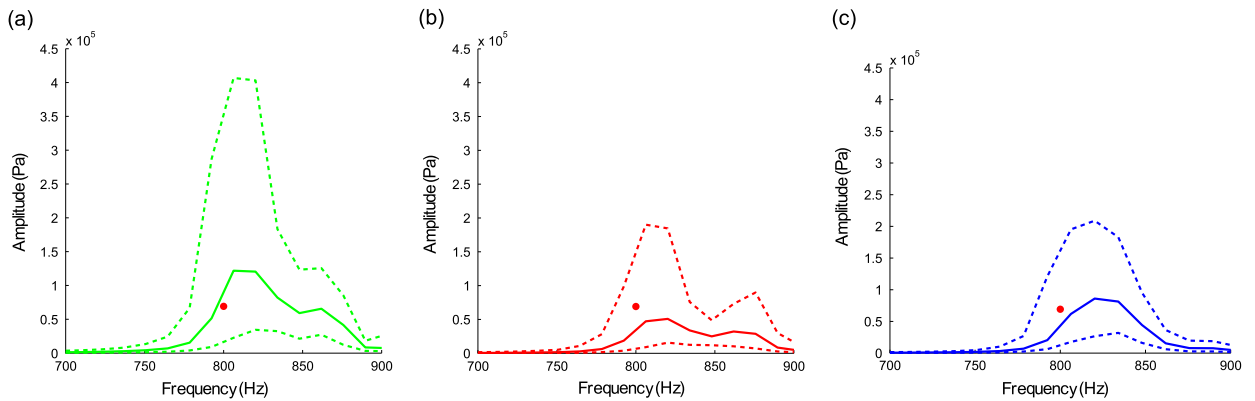
(a)

(b)

(c)

Fig. 14. Median spectrum (–) and the first and third quartiles (– –) estimated from 1000 MC simulations of 800 Hz passing-by sources at 320 km/h with a 10 dB SNR. The results are obtained from the dedopplerised beamforming using (a) the spiral array, (b) the star array and (c) the c_{iso} optimised array. The source frequency and power are indicated by the ●.

The position of a harmonic source at 800 Hz is randomly drawn. Two other sources are diametrically opposite drawn on a 1.1 radius circle centred on the first source. A 320 km h^{-1} motion is applied parallel to the plane of the array (as shown in Fig. 1(a)). White noise is added to the simulated array measurements with a 10 dB SNR. This simulation can be related to a source configuration on the train. The dedopplerised beamforming is applied to the position of the centred source on a distance of 6 m, as in Section 2, leading to a resolution of $\Delta_f = 14$ Hz. The source trajectory is 4 m from the array. This configuration of the sources simulates the passing by of a train.

The results are presented in Fig. 14 in terms of median spectrum and first and third quartiles computed over 1000 MC simulations with the spiral array, star array and c_{iso} optimised array respectively. The amplitude and frequency of the source to identify are indicated by the ●.

The spiral and star arrays produce a high sidelobe at 870 Hz corresponding to the highest Doppler frequency of the other sources. For the optimised array, no sidelobe is present. One can notice that the exact frequency is not recovered by any of the arrays; the maxima are located between 806 Hz and 820 Hz. Concerning the estimation of the source power, the median curves of the optimised and spiral arrays are the closest to the real values. However the optimised array has a narrower quartile dispersion.

These simulations point out that the beampattern optimisation may enhance the source separation. The optimisation of c_{iso} criterion leads to a better separation ratio and a better correction of the Doppler effect. In the next section, real data, acquired from an array optimised according to c_{iso} criterion and built for the experiment, are processed to apply the source imaging technique to a high speed train.

6. Application to high speed train

The c_{iso} optimised array (see Fig. 12(a) and its dedicated support in Fig. 15) and the star array, whose geometry is plotted in Fig. 1(a), are used to localise the source on a high speed train (TGV). The first array is optimised from a 3 m × 3 m grid with a 2.5 cm spacing. The train is passing at 320 km h^{-1}. The arrays are 4 m distant from the external line of the rail. The beamformer outputs are presented for third-octave bands centred on 700 Hz, 1080 Hz and 1280 Hz in Figs. 16, 17 and 18.

Note that beamforming may not identify correctly the rail radiation [29]. Adapted array processing has been proposed considering the radiation of periodically supported beam [30], but its application to moving scenarios remains difficult. Also, the ground reflections are not taken into account in the present study.

The sources at 700 Hz for the c_{iso} optimised array and the star array, respectively shown in Fig. 16(a) and (b), are mainly located around the first bogie for both arrays ($x=0$ m and $z=0$ m). Less powerful sources are located at the second bogie and for the optimised array under the sixth wheel. For this frequency, the arrays localise the same sources with the same relative amplitudes.

At 1080 Hz in Fig. 17, the main sources are located around the wheels (vibroacoustic sources) and around the louvers (aeroacoustic sources located between 10 and 15 m along the train and at 2 m high). The optimised array more accurately localises the noise radiated by the wheels. The first wheel is the loudest source highlighted. As the size of the spots of higher sound level in the mapping given by the c_{iso} array is smaller than those given by the star array and as these spots are more easily associated with noisy elements of the train according to the SNCF railway experts, it appears that the localisation from the optimised array presents a better accuracy than the star array, especially for the noise radiated by the wheels.

The c_{iso} optimised array also localises the sources more accurately than the star-shaped array in the 1280 Hz centred bandwidth, as indicated in Fig. 18. Similar tendencies are observed: wheels are identified as the main sources, especially the first one. The pantograph cavity on the top of the train at 15 m appears clearly as an aeroacoustic source whereas its contribution is not detected by the star array in Fig. 18(a). The sources generated by the louvers are not well localised on the train
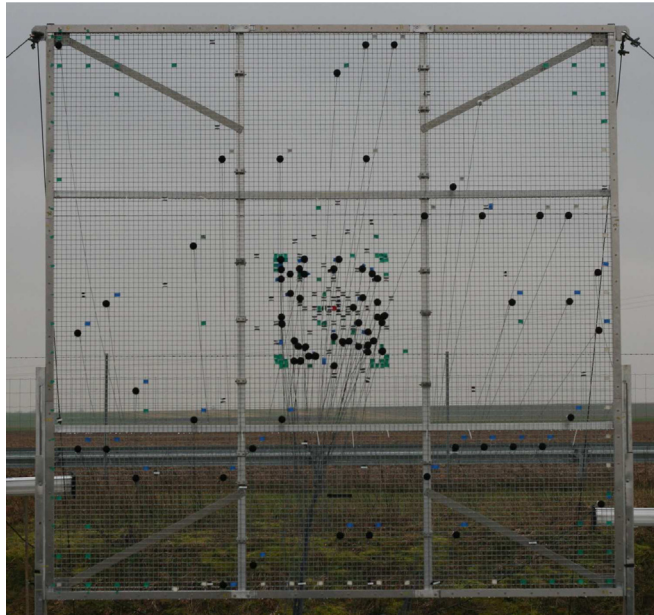
Fig. 15. Optimised arrays according to the c_{iso} criterion for the [200 1200] and [1200 8000] Hz frequency bands. The second one is delimited by green squares in the middle of the picture. The black-filled circles are the microphones. (For interpretation of the references to colour in this figure caption, the reader is referred to the web version of this paper.)
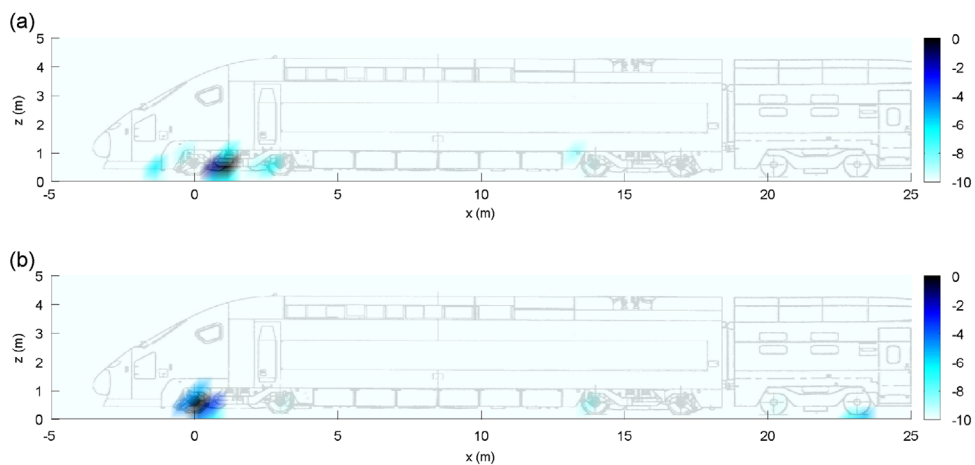

Fig. 16. 700 Hz beamforming results for a high speed train (TGV) at 320 km h^{-1}. They are obtained using the algorithm in [8] from the (a) star-shaped array and (b) the c_{iso} optimised array.

due to its large dimension and the use of a point source model. Also, a source appears in Fig. 18(a) above the train and cannot be related to a physical phenomenon.

This application highlights that the localisation may be improved using an adapted array. Interference has been removed and the localisation seems more accurate. This example validates the performance observed on the simulations.

7. Conclusions

This paper introduces a genetic algorithm method to optimise the geometry of the array built for moving source localisation by beamforming processing. The beamwidth, the maximum sidelobe level and their combination are used as cost functions. An isotropic function is introduced by minimising the relative standard variation of the cost functions for several focussing points which is of particular significance for the imaging of high speed moving vehicles.

The algorithm convergence is validated and expected properties are observed: a large array increases the beamwidth and concentrated sensors reduce the sidelobes. An original geometry is obtained for the isotropic optimisation: the sensors seem to be grouped as sub-arrays. The performance of this array is estimated in realistic Monte Carlo simulations and compared
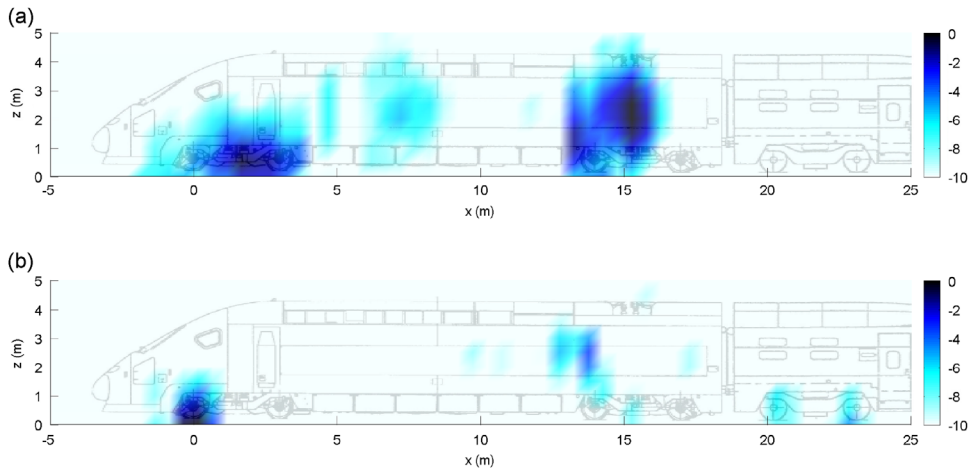
Fig. 17. 1080 Hz beamforming results for a high speed train (TGV) at 320 km h^{-1}. They are obtained using the algorithm in [8] from the (a) star array and (b) the c_{iso} optimised array.
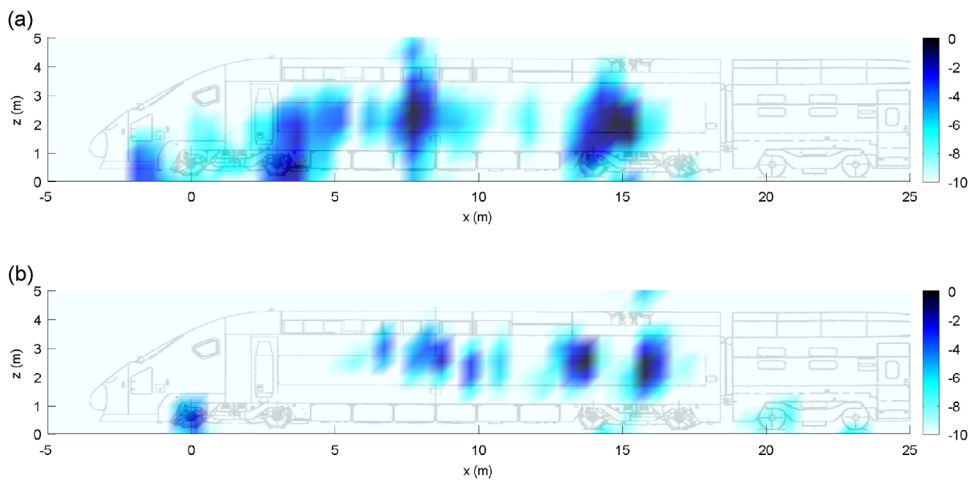

Fig. 18. 1280 Hz beamforming results for a high speed train (TGV) at 320 km h^{-1}. They are obtained using the algorithm in [8] from the (a) star array and (b) the c_{iso} optimised array.

to classic array designs. The optimised array exhibits a great ability to separate two sources for a large frequency band and to recover the emitted frequency of a moving source. Those two properties are of major concern for imaging moving sources. This is illustrated for a high speed train, where the use of the optimised array provides accurate source localisation. Since the beampattern of this array has a low spatial variance, application of the deconvolution algorithm becomes more appropriate. The optimisation algorithm is of interest since it may be easily improved and new criteria can be introduced. In a general point of view, it is relevant for providing geometry adapted to a particular application in a specific frequency bandwidth.

Acknowledgements

References

[1] L. Fritschi, L. Brown, R. Kim, D. Schwela, S. Kephalopolous, *Burden of Disease from Environmental Noise: Quantification of Healthy Years Life Lost in Europe*, World Health Organization, Geneva, Switzerland, 2011.
[2] D.H. Johnson, D.E. Dudgeon, *Array Signal Processing: Concepts and Techniques*, Simon & Schuster, New York, United states, 1992.
[3] F. Le Courtois, F. Poisson, J.-H. Thomas, J.-C. Pascal, Sound sources characterization on a high speed train from microphone array measurements, *Proceedings of Inter-Noise 2011*, Osaka, Japan, 2011.

[4] C. Mellet, F. Létourneaux, F. Poisson, C. Talotte, High speed train noise emission: *latest investigation of the aerodynamic/rolling noise contribution*, *Journal of Sound and Vibration* 293 (3–5) (2006) 535–546.

[5] H. Kook, G.B. Moebs, P. Davies, P.S. Bolton, An efficient procedure for visualizing the sound field radiated by vehicles during standardized passby tests, *Journal of Sound and Vibration* 233 (1) (2000) 137–156.

[6] V. Fleury, J. Bulté, Extension of deconvolution algorithms for the mapping of moving acoustic sources, *Journal of the Acoustical Society of America* 129 (3) (2011) 1417–1428.

[7] S. Oerlemans, P. Sijtsma, B. Méndez López, Location and quantification of noise sources on a wind turbine, *Journal of Sound and Vibration* 229 (4) (2007) 869–883.

[8] B. Barsikow, On removing the Doppler frequency shift from array measurements of railway noise, *Journal of Sound and Vibration* 120 (1) (1988) 190–196.

[9] T.F. Brooks, W.M. Humphreys, A deconvolution approach for the mapping of acoustic sources (damas) determined from phased microphone arrays, *Journal of Sound and Vibration* 294 (4) (2006) 856–879.

[10] T. Suzuki, L 1 generalized inverse beam-forming algorithm resolving coherent/incoherent, distributed and multipole sources, *Journal of Sound and Vibration* 2330 (24) (2011) 5835–5851.

[11] J.A. Högbom, Aperture synthesis with a non-regular distribution of interferometer baselines, *Astronomy and Astrophysics Supplement Series* 15 (1974) 417–426.

[12] R.P. Dougherty, Functional beamforming, *Proceedings of the Berlin Beamforming Conference*, Berlin, Germany, 2014.

[13] F. Le Courtois, Caractérisation des sources acoustiques sur le matériel ferroviaire par méthode d'antennerie, PhD Thesis, Université du Maine, 2012.

[14] F. Le Courtois , J.-H. Thomas, F. Poisson, J.-C. Pascal, Méthode de déconvolution pour l'imagerie des sources en mouvement rapide, *Proceedings of Congrès français d'Acoustique*, Poitiers, France, 2014.

[15] J.J. Christensen, J. Hald, Beamforming, Technical Review No. 1 - 2004, Brüel and Kjær Sound and Vibration Measurements A/S, 2004.

[16] A. Nordborg, J. Wedemann, L. Willenbrick, Optimum array microphone configuration, *Proceedings of Inter-Noise*, Nice, France, 2000.

[17] A. Moffet, Minimum-redundancy linear arrays, *IEEE Transactions on Antennas and Propagation* 16 (2) (1968) 172–175.

[18] Y. Tanako, X-shaped two-dimensional microphone array system for measuring noise-source distribution on moving vehicles, *JSME International Journal Series C* 1 (41) (1998) 46–50.

[19] E. Tiana-Roig, F. Jacobsen, E.F. Grande, Beamforming with a circular microphone array for localization of environmental noise sources, *Journal of the Acoustical Society of America* 6 (128) (2010) 3535–3542.

[20] R.P. Dougherty, Spiral-shaped array for broadband imaging, U.S. Patent No. 5,838,284, U.S. Patent and Trademark Office, Washington, DC, 1998.

[21] J. Underbrink, Beamforming in acoustic testing, in: T.J. Mueller (Ed.), *Aeroacoustic Measurements*, Springer-Verlag, Berlin, Germany2002, p. 98.

[22] H. Kook, P. Davies, J.S. Bolton, Statistical properties of random sparse arrays, *Journal of Sound and Vibration* 255 (5) (2002) 819–848.

[23] S. Holm, A. Austeng, K. Iranpour, J. Hopperstad, Sparse sampling in array processing, in: F. Maravasti (Ed.), *Sampling Theory and Practice*, Plenum, New York, United States, 2001.

[24] R.L. Haupt, Thinned arrays using genetic algorithms, *IEEE Transactions on Antennas and Propagation* 42 (1994) 993–999.

[25] G. Elias, C. Malarmey, Utilisation d'antennes focalisées pour la localisation des sources acoustiques, *Proceedings of the 11th International Conference on Acoustics*, Paris, France, 1983, pp. 163–166.

[26] J. Holland, *Adaptation in Natural and Artificial Systems*, 2nd edition, MIT Press, Cambridge, United States, 1992.

[27] Z. Michalewicz, *Genetic Algorithms + Data Structures = Evolution Programs*, *Artificial Intelligence*, 3rd edition, Springer, Berlin, Germany, 1996.

[28] R. Poli, W. Langdon, N. McPhee, J.R. Koza, A field guide to genetic programming, Lulu.com, 2008.

[29] T. Kitagawa, D.J. Thompson, Comparison of wheel/rail noise radiation on Japanese railways using the TWINS model and microphone array measurements, *Journal of Sound and Vibration* 293 (3) (2006) 496–509.

[30] B. Faure, O. Chiello, M.-A. Pallas, C. Servière, Characterisation of the acoustic field radiated by a rail with a microphone array: the SWEAM method, *Journal of Sound and Vibration* 346 (3) (2015) 165–190.